Journal of the Ceramic Society of Japan 124 [10] 1067-1071 2016 Full paper

Fabrication of cellular and lamellar $LiFePO_4$/C Cathodes for Li-ion batteries by unidirectional freeze-casting method

Sara ZAVAREH,† André HILGER,* Kathrin HIRSELANDT, Oliver GOERKE, Ingo MANKE,* John BANHART* and Aleksander GURLO

Fachgebiet Keramische Werkstoffe/Chair of Advanced Ceramic Materials, Technische Universität Berlin, Hardenbergstr. 40, 10623 Berlin, Germany
***Institute of Applied Materials, Helmholtz Centre Berlin for Materials and Energy, Hahn-Meitner-Platz 1, 14109 Berlin, Germany**

Highly porous lamellar and cellular cathodes for Li-ion batteries were fabricated from additive-stabilized aqueous suspensions of lithium iron phosphate and carbon black by the unidirectional freeze-casting method and characterized by optical microscopy, scanning electron microscopy, mercury porosimetry, helium pycnometry and X-ray microtomography. The size and orientation of the pores in the specimens were controlled through the variation of the freezing parameters. The diameters of the pores, which are in the range from 0.7 to 30 μm, as well as the wall thickness, decrease as the cooling rate increases. Pore volume and total porosity increase while the solid content of the suspension decreases. The specimen's structure was changed from lamellar to cellular by increasing the gelatin concentration and solid content in the suspensions. The lamellar specimens demonstrate higher porosity (82–84%) than the cellular samples. Cathodes with lamellar structure possess higher specific capacity and less loss of energy density in comparison to those having cellular structure.

Key-words : Li-ion batteries, Cathodes, Freeze-casting, Ice-templating, Porosity, Electrochemical performance

[Received May 13, 2016; Accepted July 28, 2016]

1. Introduction

As the diffusion of Li-ions plays an important role for the electrochemical performance of Li-ion batteries (LIBs), the design of a suitable electrode microstructure is a current approach to achieve high diffusion rates and, therefore, high power densities in LIBs.[1] Hierarchical porous structure of materials can provide efficient ion transport pathways due to the more effective adsorption of the electrolyte.[2),3] A large electrolyte/electrode interface results in a rapid charging rate of LIBs. Moreover, the stress in the cells caused by the charging and discharging of batteries is generally relaxed in a porous structure consisting of small particles.[4]

Freeze-casting is one of the most promising and cost-effective techniques for the fabrication of macroporous ceramics. This technique, also known as ice-templating, relies on the formation and subsequent sublimation of ice crystals that act as pore templates in frozen particulate dispersions.[5] In a typical freeze-casting process a particulate dispersion is frozen under controlled conditions, after which the pores are formed during sublimation of solvent. The freeze-casting technique provides several advantages over other templating methods, including: (i) freeze-casting is a simple and low-cost technique; the pores are generated by environmentally friendly agents and not by polymer burnout stage during sintering, reducing the production time and costs as well as carbon contamination of the ceramics, (ii) the control of the solidification process and of the growth of ice crystals allows for the control of the geometry of pore space since the latter is directly templated by ice crystals in the frozen specimens, and (iii) macroporous ceramics fabricated via the freeze-casting method exhibit low shrinkage in comparison to those fabricated by other techniques.[6),7] Freeze-casting has been applied to the processing of macroporous ceramics for solid oxide fuel cells,[8)–12] electrical energy storage,[4),6),13)–16] membranes[17),18] as well as of bioceramics[19)–26] and piezoceramics.[27),28] Up to now, only few publications report on freeze-cast electrodes for LIBs. A highly porous $LiFePO_4$/C cathode with a total porosity of 88% was fabricated by a combined gelation and freeze-casting method, called 'gelation freezing'.[4] This method allowed for generating cellular (honeycomb-like) structures with cylindrical pores with an average pore size of 250, 140 and 70 μm for the specimens frozen at −40, −60, and −80°C, respectively. The electrochemical performance of the cells was strongly influenced by pore sizes, i.e. the specific capacity of cathodes decreased with decreasing pore diameter that in turn decreased with decreasing freezing temperature. Another work addressed nickel cobalt aluminum oxide (NCA) cathodes with a lamellar pore structure that showed capacity loss at high cycling rates.[29] Due to the differences between the materials ($LiFePO_4$ and NCA), a direct comparison between different pore geometries is impossible. Therefore the goal of this work is to fabricate macroporous $LiFePO_4$/C cathodes with both cellular and lamellar pore geometries and to compare their electrochemical performance.

2. Experimental procedure

2.1 Fabrication of the $LiFePO_4$/C specimens

A $LiFePO_4$/C suspension was prepared by mixing $LiFePO_4$ (LFP, Life Power® P2 Phostech Lithium, Clariant) with Carbon Black (CB, Super P Conductive, 99+%, Alfa Aesar) in the weight ratio 95:5, a proper amount of a dispersant (DISPERBYK-190,

† Corresponding author: S. Zavareh; E-mail: sara.zavareh@ceramics.tu-berlin.de
‡ Preface for this article: DOI http://dx.doi.org/10.2109/jcersj2.124.P10-1

DOI http://dx.doi.org/10.2109/jcersj2.16126

Table 1. Processing parameters for the fabrication of specimens with lamellar and cellular structures

Samples	Solid Content (wt.%)	Gelatin Concentration (wt.%)	Cooling Rate (K/min)	Suspension Temperature (°C)
Cellular	40	2.4	2	25
Lamellar 1	30	1.8	2	25
Lamellar 2	30	1.8	6	25

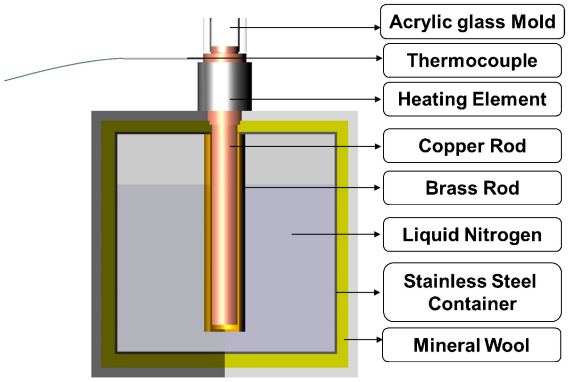

Fig. 1. The schema of the self-made freeze-casting set-up.

Byk) and a binder (1.8–2.4 wt %) in deionized water. This mixture was stirred and homogenized by sonication (SONOREX, Bandelin) for 30 min. Sodium silicate (Na_2O: 7.80–8.50%, SiO_2: 25.80–28.50%; Carl Roth), modified butadiene-styrene copolymer (WSB™; ZEON Corporation) and gelatin (from porcine skin, 170–195 g Bloom, medium gel strength for microbiology; Sigma Aldrich) were used as binders. The binder solution was added to the LFP-CB suspension, stirred on a magnetic stirrer for 30 min and finally de-aired under vacuum. The suspension was poured into a mold and cooled from ambient temperature (~25°C) to −95°C at rates of 2 and 6 K/min until the samples were fully solidified. After this, the solidified samples were dried in a freeze dryer under vacuum (~0.08 mbar) at 20°C for 24 h. **Table 1** displays the processing parameters for the fabrication of specimens with lamellar and cellular structures.

2.2 Freeze-casting set up

The freeze-casting experiments were carried out in an adapted self-made freeze-casting setup (see **Fig. 1**) and a commercial freeze-dryer (Christ Gamma 2–20, Martin Christ Gefriertrocknungsanlagen GmbH, Germany). The freeze-casting setup consists of a stainless steel container for liquid nitrogen (cooling medium), mineral wool isolation, a brass rod, a copper rod, a heating element, an acrylic glass mold and a thermocouple. The brass rod aids in avoiding direct contact of the copper rod with liquid nitrogen and in achieving a more controlled freezing process. Dipping the copper rod directly into liquid nitrogen did not lead to a well-controlled cooling rate, because insufficient power was supplied to heat the copper rod in order to maintain the fixed cooling temperature and linear freezing rate. Thus, there is an air gap between the copper rod and brass rod, which allows for applying a linear cooling rate. The copper rod transports the coldness from the liquid nitrogen container to the suspension, which has been poured into an acrylic glass mold. A heating element on top of the copper rod allows to control the temperature gradient and to establish a linear cooling rate. For unidirectional solidification, the ceramic suspension must be cooled just from one side and the ice crystals must start growing from the cooling surface of the copper rod. For this reason, a mold made of acrylic glass with a very low thermal conductivity (~0.2 $W \cdot m^{-1} \cdot K^{-1}$) was used. Acrylic glass is also transparent, which allows for assessment during freezing of whether the solidification process has terminated completely.

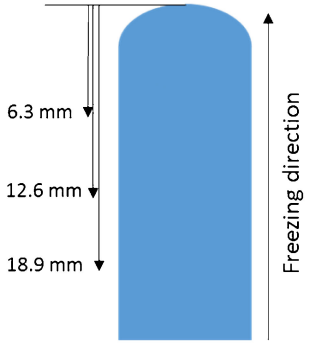

Fig. 2. Locations of the horizontal cross-sections for computer tomography characterization. Distances from the top are 6.3, 12.6 and 18.9 mm.

2.3 Characterization methods

2.3.1 Optical microscopy

A rapid qualitative characterization of the pore structure and orientation in the specimens was performed by UV-based optical microscopy with a Leica DM 4000 M (Leica Microsystems, Germany). The specimens were infiltrated under vacuum with a mixture of resin (EpoFix resin, Struers) and fluorescing powder (EPODYE, Struers). A thin slice oriented parallel to the solidification direction was cut out from the infiltrated specimens with a diamond saw.

2.3.2 Scanning electron microscopy

SEM (Philips XL20, FEI, USA) was used to characterize the cross-sectional microstructure of the specimens in the slices cut out with a diamond saw perpendicular to the freezing direction. The cropped slices were fixed on the sample holders using carbon pad glue and vapor-coated with carbon to improve their electrical conductivity.

2.3.3 Mercury porosimetry

Bulk density (ρ_b) and total pore volume of the specimens were measured by mercury porosimetry with a Porosimeter 2000 WS (Carlo Erba, Germany).

2.3.4 Helium pycnometry

Particle density (ρ_p) of the specimens was measured with a Micromeritics Multivolume Gas Pycnometer 1305 (Micromeritics Instrument Corporation, USA).

The total porosity of specimens (P) was calculated according to:

$$P = 100\% \times \left(1 - \frac{\rho_b}{\rho_p}\right).$$

2.3.5 X-ray tomography

To obtain three-dimensional information of the whole interior of the prepared samples, X-ray tomographic investigations were performed. We analyzed the structural homogeneity within the entire volume and obtained cross sections at three different locations as indicated in **Fig. 2**. The used setup consists of a Hamamatsu flat panel detector (C7942SK-05) with 2316 × 2316 pixels (pixel size 50 × 50 μm^2) and a Hamamatsu microfocus X-ray tube (L8121-3). A target spot with a diameter of 7 µm was established in the experiments. The X-ray tube was operated at

100 kV voltage and 150 µA current. An exposure time of 1.1 s for each of the 1200 radiographic projection images over 360° was applied. After image acquisition, the images were used to reconstruct a 3D data set of the interior structure of the samples using the software 'Octopus'. The 3D data was analyzed with the software 'VGStudioMAx'.

2.3.6 Fabrication of electrochemical cells and characterization of electrochemical performance

For testing the electrochemical performance, cathodes in the shape of cylindrical sheets with a thickness of 0.5 and 0.8 mm for lamellar and cellular specimens, respectively, were cut out from the cylindrical specimens perpendicular to the freezing direction and dried in a dryer under argon gas at 100°C overnight. The cathodes were then brought into a glovebox to assemble Swagelok-type half-cells. Metallic lithium foil and glass microfibers were used as an anode and a separator, respectively. The electrolyte was prepared by dissolving 1 M $LiPF_6$ in a mixture of ethylene carbonate (EC) and dimethyl carbonate (DMC) in a volume ratio of 1:1. The cells were tested applying a battery cycling test program with Yokogawa GS610 (Yokogawa Deutschland GmbH, Germany) between 2 and 4 V at a cycle rate of 0.5 C/h at 1.0 mA. Specific capacity (capacity per unit weight of the active electrode material) was determined for the second charge–discharge curve.

3. Results and discussion

3.1 Choice of additives

Application of different additives and variation of freezing parameters allows to adjust the geometry of the pores in $LiFePO_4$/C cathodes. **Figure 3** displays the pore structure of specimens fabricated without additives and with sodium silicate, WSB and gelatin under the same freezing conditions. The specimen fabricated without additive exhibits an irregular pore structure; this specimen was not stable enough to be demolded after sublimation. The dendrite-like structures [marked by arrows in Figs. 3(b) and 3(c)] were observed in the specimens freeze-cast with WSB and sodium silicate. The gelatin inhibits the growth of ice dendrites, allowing for fabrication of macroporous specimens with a well-defined lamellar pore structure as seen in Fig. 3(d). Therefore, the specimens fabricated with gelatin were selected for further studies.

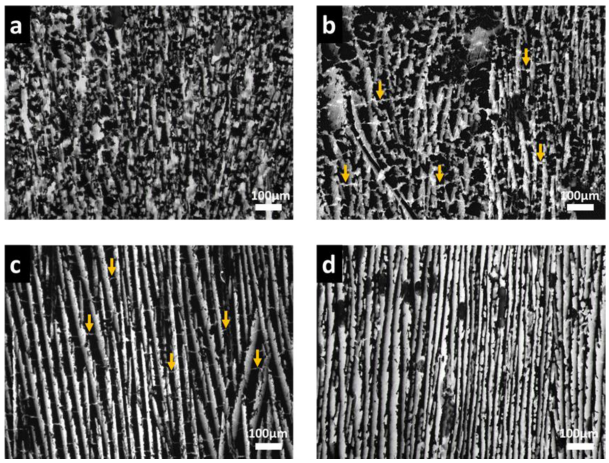

Fig. 3. UV optical micrographs of freeze-cast specimens fabricated without binder (a), with WSB (b) with sodium silicate (c) and with gelatin (d). The arrows point at the dendrites.

3.2 Fabrication of specimens with cellular and lamellar pore structures

In the next step, the solid content, gelatin concentration and cooling rate were varied in order to fabricate specimens with cellular and lamellar structures. The variation of cooling rate differs in the thickness of $LiFePO_4$/C walls as well as in pore diameter. **Figure 4** displays the micrographs of the cross-sections of the fabricated porous specimens. The specimens with a lamellar pore structure exhibit plate-like pores and solid walls. Growth of the dendrites was observed on one side of the walls perpendicular to the temperature gradient. An increase in cooling rate from 2 to 6 K/min decreases the wall thickness and the pore diameter. On the other hand, an increase in the gelatin concentration from 1.8 to 2.4 wt.% and increasing the solid content to 40 wt.% results in the formation of cellular ceramics with honeycomb-like pores and dense solid walls.

3.3 Porosity

The specimens with cellular and lamellar structures fabricated under different processing conditions differ also in their total porosity (and density) as well as in pore size. **Figure 5** shows the results of Hg porosimetry measurements. The lamellar specimens are more porous, have a narrow pore size distribution with pore diameters in the rage of 0.7–25 µm in comparison to the cellular specimen (2–30 µm). This can be explained by a higher water content of the suspensions used for the fabrication of lamellar specimens compared to cellular specimens. Due to the fact that the pores originate from the ice crystals after sublimation, the water content plays a crucial role for the total porosity of the specimens. As indicated in **Table 2**, the cellular specimen has a higher density due to its lower pore volume. However, the skeleton density of both lamellar and cellular specimens are in good agreement due to the utilization of the same materials.

3.4 Microstructure

In order to obtain a full picture of the three-dimensional interior structure, all three samples were characterized by X-ray micro tomography (µCT). **Figure 6** shows the structure of all three specimens. Three horizontal cross sections through the tomogram of the specimens at different heights of the cylindrically fabricated specimens and the vertical cross section (parallel to the temperature gradient) reveal strong differences in the local structure at different locations.

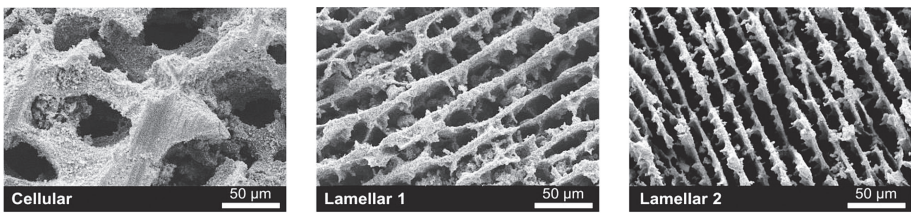

Fig. 4. SEM micrographs of freeze-cast specimens with cellular and lamellar structures studied in this work.

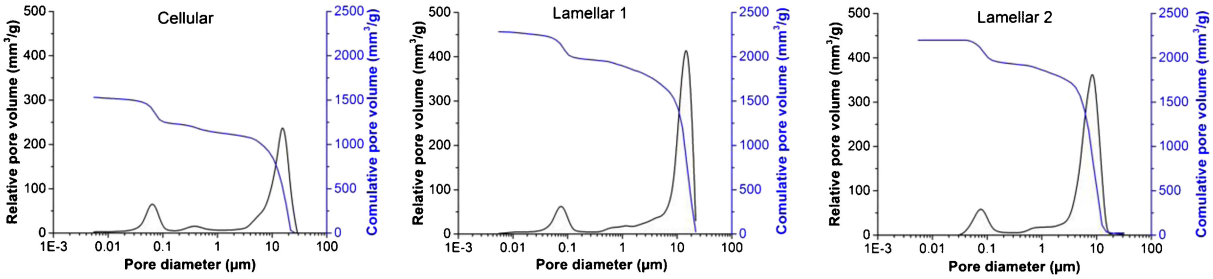

Fig. 5. Pore size distribution and pore volume of cellular and lamellar specimens.

Table 2. Open porosity, experimental density and total pore volume of the specimens

Samples	Particle Density (g/cm^3)	Bulk Density (g/cm^3)	Total Porosity (%)	Pore Volume (mm^3/g)
Cellular	2.6	0.59	77	1532
Lamellar 1	2.4	0.39	84	2283
Lamellar 2	2.4	0.43	82	2200

For all three specimens, the pore sizes strongly decrease from the top to the bottom. While the pores in the top cross section (6.3 mm from top, see Fig. 2) are clearly visible, the sizes of the pores at the bottom are close to the limit of the spatial resolution of the tomographic imaging technique (~10 µm).

As already shown with the SEM micrographs in Fig. 4 the specimens have pronounced different structures. This is confirmed by the µCT results for the whole volume. The lamellae have different orientations in space, but are mostly vertically aligned to the center axis of the cylinder. They can extend several millimeters into the sample.

The structural features of specimen 'Lamellar 1' are comparable to specimen 'Lamellar 2'. The lamellar structure is homogenously distributed along the horizontal slices but pores between the lamellae become much larger at the top.

3.5 Electrochemical performance

The freeze-cast $LiFePO_4$/C cathodes with various pore structures (cellular and lamellar) demonstrate different electrochemical performance as confirmed by the cycling curve analysis given in **Fig. 7**. It can be seen that porous lamellar cathodes demonstrate higher specific capacity in comparison to cellular cathodes under the same cycling regime.

The cellular cathode shows a plateau of the charging curve at higher voltage and a larger voltage difference between the plateaus of its charge–discharge curves. This could be related to ohmic resistance of the cellular cathode due to its thickness. This leads to more loss of energy density in the battery as well as its cycling life time. Since the cellular cathode possesses a higher amount of active material, a higher specific capacity of the battery was expected, which was in contrast to the result of the electrochemical performance. This reveals that the structure of the pores, total pore volume and the thickness of the cathode play a determining role in ionic transport during charge and discharge in the cell. This may also explain the plateau at a higher voltage during charge and a drastic decline of voltage during discharge.

The lamellar cathodes reach the specific capacity of ~126 mAh/g and indicate a similar cycling behavior with the same range of voltage difference during discharge. The plateaus of the charge and discharge curves of lamellar cathodes are longer and

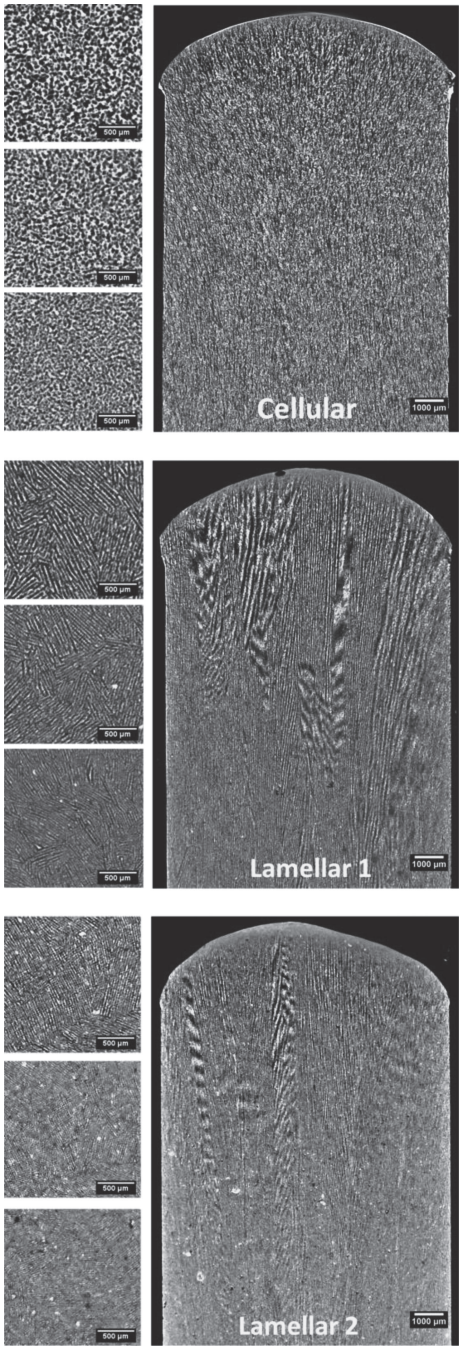

Fig. 6. X-ray micro-tomography. Top: Three horizontal cross sections (left side) through the tomogram of the cellular specimen at defined locations as indicated in Fig. 2 and a vertical cross section (right side). Center: Same for specimen Lamellar 1. Bottom: Same for specimen Lamellar 2.

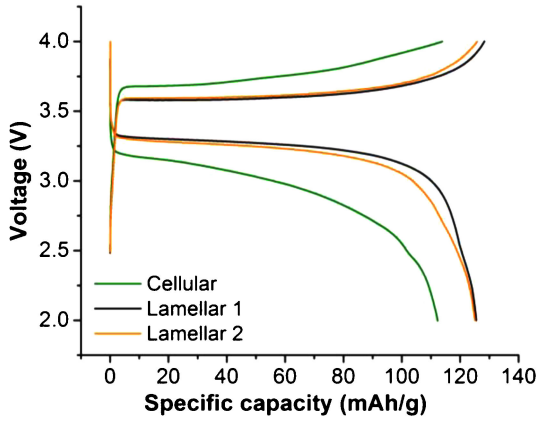

Fig. 7. The second charge–discharge curve of the lamellar and cellular freeze-cast LFP-CB cathodes.

Table 3. Characteristics of the tested cathodes

	Cellular	Lamellar 1	Lamellar 2
Thickness (mm)	0.8	0.5	0.5
Weight (mg)	19.3	14.2	16.4
Weight of the active material (LFP/C) (mg)	16.8	12.4	14.3
Specific capacity[a)] (mAh/g)	115	126	126

a) capacity per unit weight of the active electrode material (LFP).

appear at lower voltage. Specimen 'Lamellar 2' shows a faster voltage decrease during discharge compared to the specimen 'Lamellar 1'. Since the ionic transport relates to the cathodes' microstructure, varying the pore size and wall diameter in cathodes with the same pore structure and the same thickness affects the electrochemical performance of a battery. However, the influence of this is rather small, as seen in Fig. 7 and **Table 3** for the 'Lamellar 1' and 'Lamellar 2' specimens.

4. Conclusions

Highly porous $LiFePO_4$/C cathodes for Li-ion batteries with well-defined lamellar and cellular pore structures have been successfully fabricated by applying the unidirectional freeze-casting technique. The well-aligned lamellar pore structure was formed by using up to 1.8 wt.% gelatin as a freezing additive and 30 wt.% of solid content. Further increase of the gelatin content to 2.4 wt.% in the slurry and the solid content to 40 wt.% leads to the formation of a cellular pore structure with a honeycomb-like morphology. The diameter of the pores as well as the thickness of the walls decrease when increasing the cooling rate from 2 to 6 K/min. The total porosity and pore volume increase with decreasing solid content, which also leads to an increase in bulk density.

Tomographic 3D images revealed a homogenous distribution of LFP-CB along the horizontal cross sections, but strong differences in the pore size between the top and the bottom section in all three samples. Pore sizes are much larger close to the top side.

This work shows that the prepared cathodes have significantly different electrochemical performance. Cathodes with a lamellar pore structure exhibit higher specific capacity and less loss of energy density than those with cellular pore structure as confirmed by cycling curve analysis.

Acknowledgments We are greatly thankful to Prof. Dr.-Ing. Julia Kowal and Dr. Maged F. Bekheet for scientific discussions and Mr. Delf Kober for his support in battery tests (all at the Technische Universitaet Berlin).

References

1) A. D. Roberts, S. Wang, X. Li and H. Zhang, *J. Mater. Chem. A Mater. Energy Sustain.*, 42, 17787–17796 (2014).
2) B. Vijayaraghavan, D. R. Ely, Y.-M. Chiang, R. García-García and R. E. García, *J. Electrochem. Soc.*, 5, A548–A552 (2012).
3) D.-W. Chung, M. Ebner, D. R. Ely, V. Wood and R. Edwin García, *Model. Simul. Mater. Sci. Eng.*, 7, 74009 (2013).
4) K. Hamamoto, M. Fukushima, M. Mamiya, Y. Yoshizawa, J. Akimoto, T. Suzuki and Y. Fujishiro, *Solid State Ionics*, 225, 560–563 (2012).
5) T. Ohji and M. Fukushima, *Int. Mater. Rev.*, 2, 115–131 (2012).
6) L. Dan and Q. Ling, Patent No. 2013000939. Australia, Aug. 23 (2013).
7) J. Han, C. Hong, X. Zhang, J. Du and W. Zhang, *J. Eur. Ceram. Soc.*, 1, 53–60 (2010).
8) Y.-H. Koh, J.-J. Sun and H.-E. Kim, *Mater. Lett.*, 6, 1283–1287 (2007).
9) Y. Chen, J. Bunch, T. Li, Z. Mao and F. Chen, *J. Power Sources*, 213, 93–99 (2012).
10) S. W. Sofie, *J. Am. Ceram. Soc.*, 7, 2024–2031 (2007).
11) J.-W. Moon, H.-J. Hwang, M. Awanoa and K. Maeda, *Mater. Lett.*, 8, 1428–1434 (2003).
12) A. Z. Lichtner, D. Jauffrès, D. Roussel, F. Charlot, C. L. Martin and R. K. Bordia, *J. Eur. Ceram. Soc.*, 2, 585–595 (2015).
13) E. Ulrich, H. Michael J., O. Rainer and W. Thomas, Patent No. 102010001631, Jun. 30 (2011).
14) C. Yet-Ming, http://energy.gov/sites/prod/files/2014/03/f11/es071_chiang_2011_o.pdf (accessed February 21, 2013).
15) R. Ranjusha, K. M. Sajesh, S. Roshny, V. Lakshmi, P. Anjali, T. S. Sonia, A. Sreekumaran Nair, K. Subramanian, S. V. Nair, K. P. Chennazhi and A. Balakrishnan, *Microporous Mesoporous Mater.*, 186, 30–36 (2014).
16) X. Xie, Y. Zhou, H. Bi, K. Yin, S. Wan and L. Sun, *Sci. Rep.*, 3, 2117 (2013).
17) C. Mu, Y. Su, M. Sun, W. Chen and Z. Jiang, *J. Membr. Sci.*, 1–2, 15–21 (2010).
18) C. Gaudillere, J. Garcia-Fayos and J. M. Serra, *J. Mater. Chem. A Mater. Energy Sustain.*, 11, 3828–3833 (2014).
19) S. Deville, *Materials (Basel)*, 3, 1913–1927 (2010).
20) S. Blindow, M. Pulkin, D. Koch, G. Grathwohl and K. Rezwan, *Adv. Eng. Mater.*, 11, 875–884 (2009).
21) X. Liu, M. N. Rahaman and Q. Fu, *Acta Biomater.*, 1, 406–416 (2011).
22) M. M. Porter, M. Yeh, J. Strawson, T. Goehring, S. Lujan, P. Siripasopsotorn, M. A. Meyers and J. McKittrick, *Mater. Sci. Eng., A*, 556, 741–750 (2012).
23) Y. Zhang, K. Zuo and Y.-P. Zeng, *Ceram. Int.*, 6, 2151–2154 (2009).
24) E. Landi, F. Valentini and A. Tampieri, *Acta Biomater.*, 6, 1620–1626 (2008).
25) X. Wu, Y. Liu, X. Li, P. Wen, Y. Zhang, Y. Long, X. Wang, Y. Guo, F. Xing and J. Gao, *Acta Biomater.*, 3, 1167–1177 (2010).
26) S. Farhangdoust, A. Zamanian, M. Yasaei and M. Khorami, *Mater. Sci. Eng., C*, 1, 453–460 (2013).
27) G. Liu, T. W. Button and D. Zhang, *J. Eur. Ceram. Soc.*, 15, 4083–4088 (2014).
28) S.-H. Lee, S.-H. Jun, H.-E. Kim and Y.-H. Koh, *J. Am. Ceram. Soc.*, 9, 2807–2813 (2007).
29) S. Behr, R. Amin, Y.-M. Chiang and A. P. Tomsia, *Ceramic Forum International*, 4, E39–E43 (2015).